BEST PRACTICE PROCEDURES ON TWO-PHASE FLOW EXPERIMENTS FOR CFD VALIDATION

K. Okamoto

The University of Tokyo

Abstract

The high-speed camera had a rapid progress in early 2000s. The C-MOS chip camera now can record 7,500 frames per second (fps) with 1M pixel image resolutions. We can capture 30,000fps images with VGA image resolution. These images have both of high-temporal and high-spatial resolutions. The two-phase flow and boiling phenomena are usually highly non-linear and need high-temporal and high-spatial resolutions to extract the physics. Therefore, the C-MOS based high-speed camera is the strong tool to extract the complicated basic structures of two-phase flows.

One of the key issues of the two-phase flows is the moving boundary. High-speed camera is the strong tool to measure the moving boundary. On the image, both of the boundary motion and tracer particle could be simultaneously measured. Therefore, if the flow field were two-dimensional, only one high-speed camera is needed to capture the structures. The interaction between the flow and moving component, e.g., bubbles, structures and droplets, were precisely evaluated using the Dynamic PIV system.

1. INTRODUCTION

The rapid progress of the high-speed camera development in 2000s leaded the quantitative visualization technique to be time-resolved measurements. The high-speed camera and high-speed laser had been applied to Particle Image Velocimetry (PIV), Dynamic PIV(Okamoto, 2003). Thus, the high-temporal and high-spatial resolution velocity information can be captured with high accuracy. Huge amount of time-resolved accurate information can be easily obtained. The quantitative high-speed visualization has two major directions, i.e., Application of high-speed camera to many flow fields and Post processing of huge amount of data.

Using the high-speed camera and high-speed laser, two-dimensional or three-dimensional velocity information can be captured in the sampling frequency of around 10kHz. Just replacing the normal camera to high-speed camera, high-temporal resolution information can be very easily captured. The sampling frequency of LDV and HWA are also around 1~10kHz, so the high-speed PIV can capture the equivalent information of 10,000 LDV or HWA with two or three-dimension.
Shinohara et al.(2006) applied the high-speed camera for micro-PIV measurement. They captured the transient micro-scale vortex at the oil/water interface. The high-speed PIV is very strong tool for micro structure analysis. Sugii et al. (2003) measured the red blood cell motion inside the mesenteric arteriole of living rat. Effects of heartbeat for the velocity distributions in 30μm arteriole were discussed. Jeong et al. (2006) measured the individual red blood cell (RBC) motion inside the 6μm capillary that is narrower than the RBC size itself. The relation between the RBC deformation and RBC velocity had been clarified. They also pointed out that the RBC entry to capillary was random process.

For the three-dimensional measurement, holographic PIV system has been modified to using the high-speed camera(Okamoto, 2004). The in-inline hologram of the particles were recorded onto the high-speed camera, then the three-dimensional velocity distributions in 20mm x 20mm x 20mm cubic area were captured in 1kHz. The 3D-PTV technique had been measured by three high-speed cameras with 70W pulse YAG laser with 1kHz to measure the time-resolved three-dimensional velocity distribution in the 100mm x 100mm x 100mm cubic area(Hwang et al., 2005).

For the micro-PIV, combining the vertical scanning direction system of microscope with high-speed camera, three-dimensional velocity distribution in 100μm tube were measured(Shinohara et al., 2005). The scalar property can be measured using high-speed camera. Ko et al. measured the density distributions using the speckle tomography technique with 3 high-speed cameras(Ko et al., 2006).
For the two-phase flow experiments, the high-speed camera and Dynamic PIV system is the strong tool to verify the CFD codes.

2. HIGH-SPEED VISUALIZATION ON DROPLET BOILING

Someya et al. (2010a) experimentally investigated the Droplets impinging on a hot surface that is near the Leidenfrost temperature. Ejection of jets from the top of the droplet was observed during the transient interaction between the droplet and a hot wall. This phenomenon is called as jet ejection from droplets. When the bottom of the droplet initially impacts the hot surface, a jet is to be ejected from the top of the droplet. The jet ejection occurred only at low impact velocities and around the wetting limit temperature. It was not observed when droplets were dropped from large heights or when the surface was at a high temperature.

Figure 1 shows the sequential images of the jet ejection phenomenon. Material was SUS304 and whose surface temperature was kept 260 deg. C, using the liquid metal pool. Water droplet with 2mm in diameter fell onto the heated SUS304 surface. The droplet attacking velocity was 0.48 m/s. Using the high-speed camera and halogen light illumination, the droplet image were recorded. The frame rate of the camera was 60,000 fps, and shutter speed was 1/250,000 sec, i.e. 4 ms. Figure 1 shows the time sequential images of the droplet after contacting the hot surface. The images were captured in every 0.017ms (60,000fps). After contacting the surface, nothing happens during the first 0.1ms. However, the boiling may occur at the bottom of the droplet. Then, a small cloud of bubbles appears at 0.15ms at the bottom. The cloud moves to upward, keeping the droplet shape to be stable. The moving velocity is about 8 m/s. The cloud diameter is about 0.5 mm, thus, Reynolds number of the cloud is about 4000, i.e., turbulent. At 0.43ms, the cloud reaches the top of droplet, then, it ejects with entraining the liquid of the droplet.

The mechanism of the jet ejection is not clear. The bubble is considered to be the vapour generated by the hot surface. It takes 0.15ms to generate the bubble. The time is thought to be the term to form a super-heated micro layer at the bottom of the droplet. Then, the nucleation at the droplet causes the rapid boiling to generate the vapor cloud. At this time, the temperature of surrounding liquid is not low, and the liquid does not move. Thus, the energy of vaporization pushes up the clouds relatively higher velocity. Although the cloud Reynolds number is 4000, the cloud moves very smoothly, without disturbing the surrounding liquid of droplet. The droplet surface is kept stable. Very small waves are visible, but it is caused by the pressure fluctuation of vaporization or contacting.

The jet ejection can be observed in the small range of droplet velocity and surface conditions, incl. Surface roughness and temperature. Numerical simulation may confirm the above mechanism. However, because of the higher non-equilibrium condition, the CFD code could not simulate the phenomenon, yet. Although the phenomenon is micro-scale, the phenomenon affects on the splay cooling or post-dryout heat transfer in macro-scale. The mechanism of the phenomenon should be investigated. Without the high-speed camera, jet ejection phenomenon may not be discovered. The application of the high-speed camera to many multi-phase flows will be important to understand the complex phenomena.

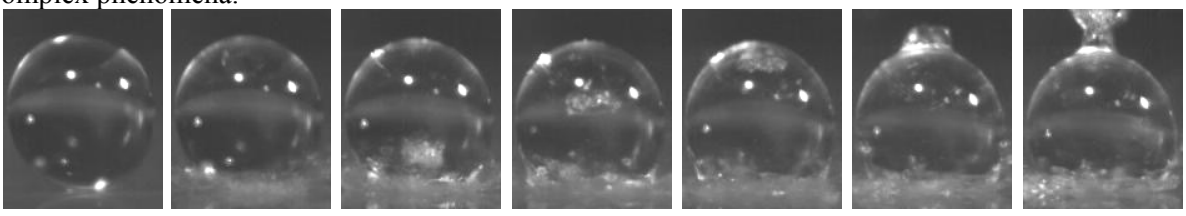

Figure 1 High-speed camera images of jet ejection (Someya et al., 2010a)

3. ESTIMATION OF PRESSURE FLUCTUATION AROUND MOVING BOUNDARY

3.1 Experimental Setup

As an example of the moving boundary, the self-induced oscillating cylinder has been evaluated. (Someya et al., 2010b)

A double pulsed Nd:YLF 527-nm wavelength laser (Pegasas PIV, NewWave Research Inc.) was used as a light source. The output power of each laser head was about 7 W, i.e. 7 mJ/pulse at 1 kHz. The maximum repetition rate of the excitation of each laser head was 5 kHz, i.e. the double-pulsed laser with two heads could provide an image pair at 5 kHz max. The laser projected a sheet of light onto the central section of the circular cylinder. Particles of ion-exchange material of approximately 63 to 150 μm in size, which absorbed fluorescent dye (Rhodamine 6G), were used as tracer particles.
The particle images were captured using a high-speed camera (Fastcam APX-RS, Photron Ltd.). This camera was capable of capturing images with a resolution of 1024×1024 pixels at a sampling frequency of 3 kHz. The spatial resolution at 10 kHz was 512×512 pixels. Thus, using a frame straddling technique, the imaging system in the present study could capture image pairs at 5 kHz max.

Figure 2 shows a schematic of the cantilever-mounted circular cylinder, 50 mm long and 10 mm diameter. One end of the circular cylinder is fixed using a stainless steel fixing pin, whilst the other end is free. Hammering tests were performed to estimate the cylinder‘s natural frequency. It was placed in quiescent fluid and hammered at 90° intervals around its circumference. As a result, the natural frequency was found to be f_0=65 Hz. In addition, the reduced damping factor was $C_n=2m\delta/\rho d^2$= 1.56, where m is the structural mass of the cylinder (7.85x10^{-3} kg/m), δ is the logarithmic decrement, and ρ is the density of water (1.0×10^{3}kg/m^3 at 20 °C).
As shown in Fig. 2(a), the fixing pin was inserted deep into the rod forming part of the structure of the cylinder. Consequently, the material of the pin affects the damping factor and the Eigen frequency of the cylinder. The experiments were conducted with the reduced velocity in the range $1.8<V_r<4.0$, at atmospheric pressure, and the Reynolds number was in the range $1.17\times10^3<Re<2.6\times10^4$. The reduced velocity V_r is dimensionless and is defined:

$$V_r = \frac{V}{f_0 \cdot d} \qquad (1)$$

where V is the mean upstream velocity of the test channel, f_0 is the natural frequency of the cylinder in the quiescent fluid, and d is the outer diameter of the cylinder.
Herein, a high temporal resolution PIV method was used to measure the velocity distribution of the flow around the circular cylinder, while the displacement of the cylinder was evaluated by image pattern matching.

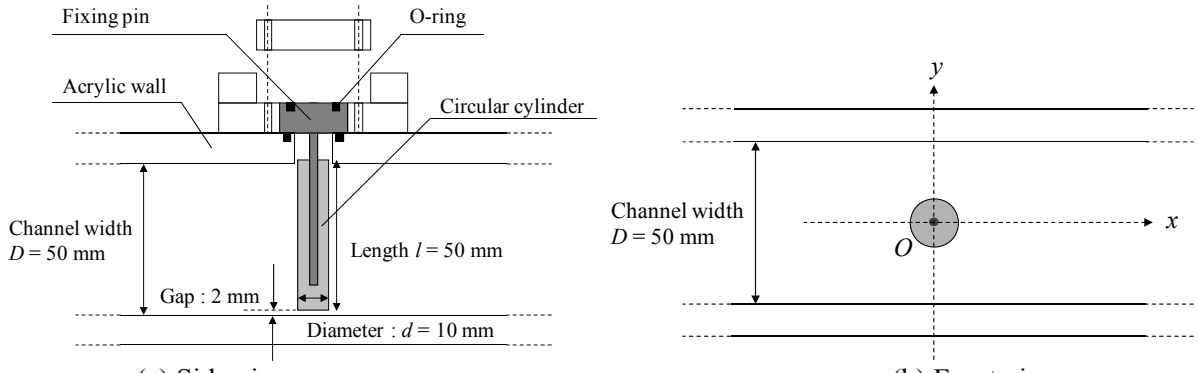

(a) Side view (b) Front view

Figure 2. Schematic diagrams of the test section (Someya, 2010b)

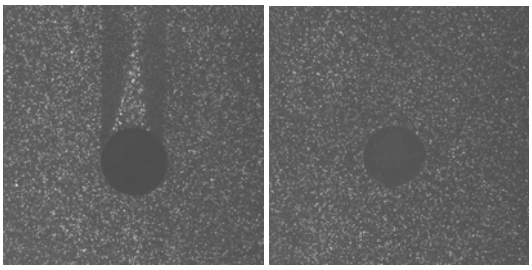

Figure 3 Area surrounding the acrylic (left) and MEXFLON (right) cylinders

A transparent acrylic resin is widely used as a material for a solid structure in these kinds of experiments. The high transparency of acrylic resin is useful, especially in flow visualization. However, its refractive index is quite different from that of water. Consequently an acrylic structure like the cylinder may cast a shadow, resulting in measurement errors. To avoid this, the refractive indexes should be matched between the fluid and structure. Herein, the refractive index of the cylinder was matched to that of water by applying MEXFLON resin. The refractive index of MEXFLON, which has high transparency, is approximately equal to that of water (Water: 1.333, MEXFLON: 1.33, Acrylic: 1.4). Consequently, optical effects from the cylinder were minimized.

Figure 3 shows photographic images around the acrylic and MEXFLON cylinders in water with suspended tracer particles. A sheet of laser light illuminates the cylinders. The image on the left shows the acrylic cylinder whilst on the right is the cylinder with MEXFLON resin. For the acrylic cylinder, the sheet of laser light is refracted at the cylinder surface resulting in a shadow behind the cylinder. Obviously, the tracer particles are invisible in this shadow. However, in the case of MEXFLON, there is no shadow and the tracer particles are uniformly visible.

3.2 Velocity and pressure distributions around moving cylinder

The Velocity distributions around the moving cylinder were measured using the PIV analysis. As the image pairs were sampled at 5 kHz, the temporal resolution was high enough to analyze the excited frequencies of the velocity field and of the cylinder with a relatively low, i.e. 65Hz. For the image processing, the uncertainties of the pattern matching and of the PIV analysis were higher than 0.1 pixels per image pair. The minimum displacement of the vibrating cylinder was around 1.6 pixels across all experiments. The largest error was about 6.3%.

Using the captured images, the instantaneous x-y positions of the circular cylinder were identified with the sampling frequency of 5kHz. The vibration amplitudes in the inline and cross-flow directions were calculated from the trajectories in the x and y directions, respectively.

Figure 4(a) shows instantaneous velocity vectors and a contour map of vorticity at V_r=2.2, where the inline oscillation dominates that for the cross-flow direction. Symmetric twin-vortices are shed behind the cylinder, accompanied by inline vibration of the cylinder. Figure 4(b) shows the velocity and vorticity distribution at V_r=4.0, where the cross-flow vibration amplitude of the cylinder becomes large. Alternating vortices were shed behind the cylinder and were synchronous with the cross-flow oscillation.

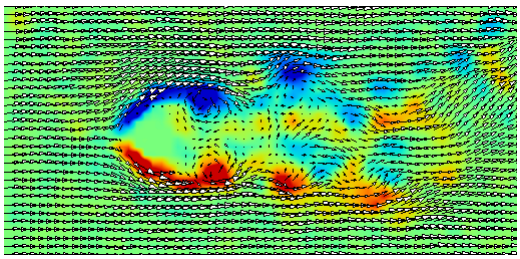

(a) Inline vibration mode
(V_r=2.2; Re=14,300).
[Symmetrical vortex pairs]

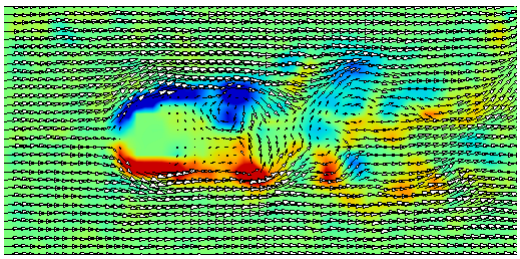

(b) Cross-flow vibration mode
(V_r=4.0; Re=26,000)
[Asymmetric vortex pairs]

Figure 4 Instantaneous Velocity & Vorticity distributions for moving cylinder (Someya 2010b)

The pressure distributions could be estimated with solving Navier-Stokes Equation using the PIV velocity data. Although the flow fields are three-dimensional, only two-dimensional information can be measured by PIV. With assuming the two-dimensional flow, the Navier-Stokes equation will have one unknown parameter, i.e., pressure.

$$\nabla^2 p = -\{\nabla \cdot (\boldsymbol{V} \cdot \nabla)\boldsymbol{V}\} + \frac{1}{\mathrm{Re}}\{\nabla \cdot \Delta \boldsymbol{V}\} \tag{2}$$

The right hand side can be calculated by the PIV velocity data, thus, Poisson equation has been solved with considering the appropriate boundary conditions. The PIV data are usually obtained with the rectangular grid system. In the self-induced oscillation cylinder system, the boundaries are moving. Therefore, setting the boundary conditions are not so easy. In this study, the polar coordinate is used instead of Cartesian coordinate because of the cylinder shape. As shown in Fig. 11(a), the cylinder images are shown as circle shape. Figure 13 shows the schematic procedure of the pressure analysis on the oscillating cylinder system. The centre of the moving cylinder is detected using the image analysis technique. The particle image is transferred to the polar coordinate system. Then, the velocity distributions are calculated using the transferred rectangular images using normal PIV technique.

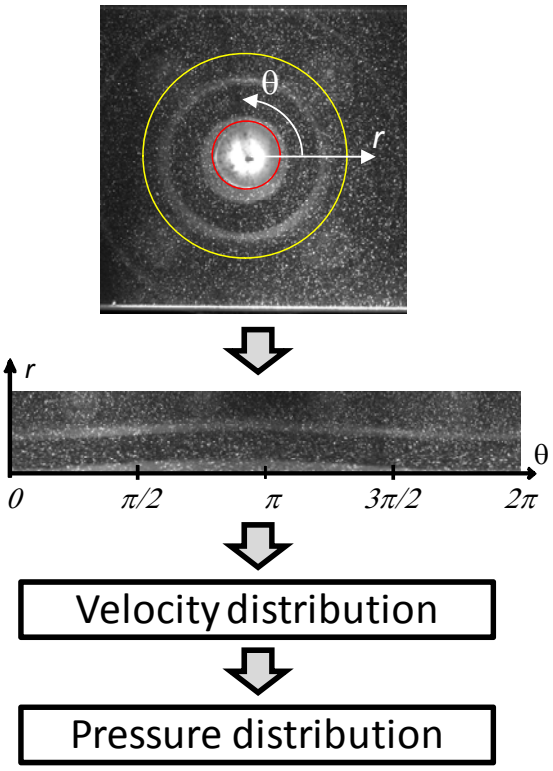

Figure 5 Procedure of pressure calculation

The right hand side of equation (2) can be rewritten with two-dimensional polar coordinate system as,

$$\begin{aligned}
&\frac{\partial^2 p}{\partial r^2} + \frac{1}{r^2}\frac{\partial^2 p}{\partial \theta^2} + \frac{1}{r}\frac{\partial p}{\partial r} \\
&= -\left[\frac{\partial}{\partial r}\left(u\frac{\partial u}{\partial r} + \frac{v}{r}\frac{\partial u}{\partial \theta}\right) + \frac{1}{r}\frac{\partial}{\partial \theta}\left(u\frac{\partial v}{\partial r} + \frac{v}{r}\frac{\partial v}{\partial \theta}\right)\right. \\
&\quad \left. - \frac{1}{\mathrm{Re}}\frac{\partial}{\partial r}\left(\frac{\partial^2 u}{\partial r^2} + \frac{1}{r^2}\frac{\partial^2 u}{\partial \theta^2}\right) - \frac{1}{\mathrm{Re}}\frac{1}{r}\frac{\partial}{\partial \theta}\left(\frac{\partial^2 v}{\partial r^2} + \frac{1}{r^2}\frac{\partial^2 v}{\partial \theta^2}\right)\right]
\end{aligned} \tag{3}$$

where p is pressure, u and v are the velocity components and r and θ are the polar coordinates. With using the obtained velocity vector, the above Poisson Equation has been solved under the appropriate boundary conditions, resulting in the pressure distributions.

Figure 6(a) shows the temporal variation of the pressure distributions for the inline vibration mode, i.e., Figure 4(a), V_r=2.2; Re=14,300. The pressure at the upstream top position, (θ=π), shows the fluctuation during the oscillation cycle. While, the pressure at the side (θ=π/2, 3π/2), the high-pressure locations are moving to downstream side in the same phase. The blue dotted lines denote the motion of low pressure regions, which represent the vortex center. The pressure distribution clearly displays the in-line vibrations.

Figure 6(b) shows the pressure distributions for cross-flow vibration mode, i.e., Figure 4(b), V_r=4.0; Re=26,000). The upstream top position (θ=π) has the almost constant pressure, which vibrates up and down, i.e., right and left in the figure. The blue dotted lines (vortex center) are not symmetrical, but periodically appears, in right and left sides (θ=0 and π). With the oscillation in cross-flow directions, the pressure distributions around the cylinder are clearly displayed.

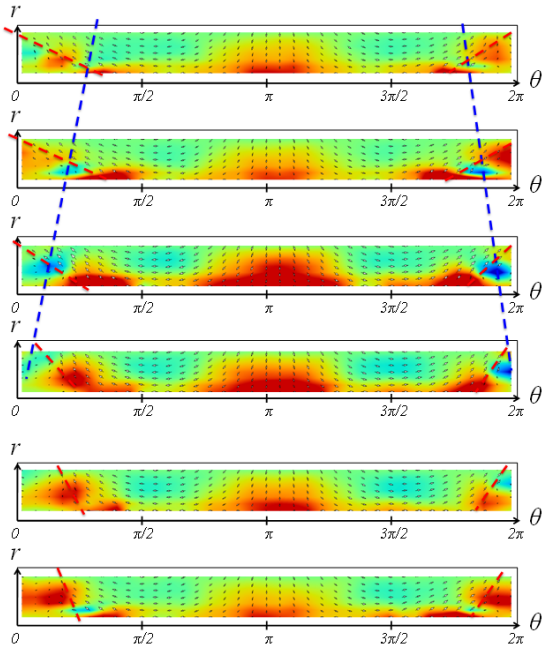

(a) in-line vibration condition.
(V_r=2.2; Re=14,300).

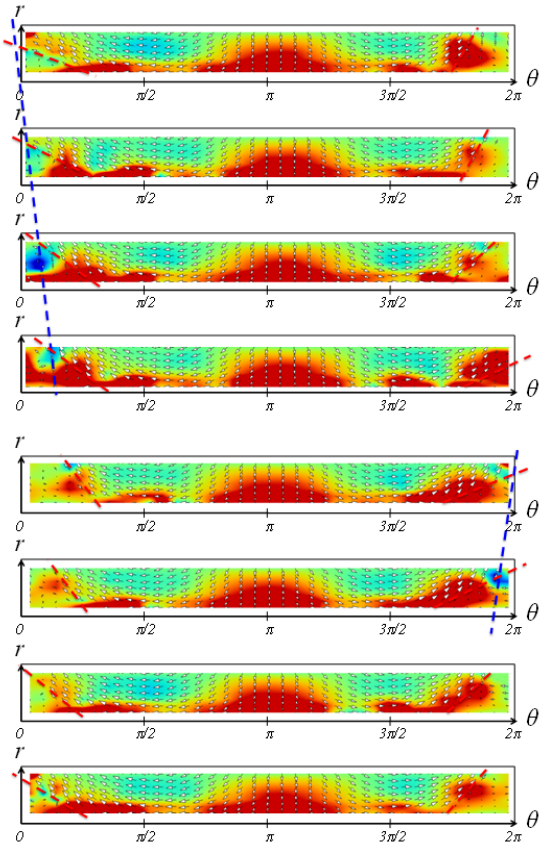

(b) cross-flow vibration condition.
(V_r=4.0; Re=26,000).

Figure 6 Pressure distribution around the moving cylinder in one cycle.

4. HIGH-SPEED MEASUREMENT ON BUBBLE LIQUID INTERACTION

4.1 Experiment

In order to investigate the interactions between the bubble and surrounding liquid, the Shadow image technique and PIV technique had been combined (Tokuhiro et al., 1998). Replacing the conventional PIV system to Dynamic PIV, and Infrared Backlight to High-speed pulse infrared laser, the transient motion of the bubbles and fluids could be easily measured (Ishikawa 2007). Figure 7 shows the schematic of the experimental setup. The simple air-bubble/water ejection tank had been used to check the applicability of the system. The Dynamic PIV system is the same with the previous section. Adding the high-speed camera and high-speed double pulse laser, we employed the high-speed infrared pulse laser (HSI-1000, Japan laser Co.). The wave length of the infrared laser is 808nm. It can generate upto 2kHz pulses. Figure 8 shows the timing chart of these 3 lasers, 2 for PIV and 1 for Shadow. The PIV pulse lasers illuminated the flow field with green color laser sheet with frame straddling technique. Short time interval was about 0.1ms, while long one was 1.9ms, so that particle image interval between the odd and even frames was 0.1ms. The time interval was short enough to capture the tracer particle motion. The infrared laser had been controlled to illuminate the shadow image at the timing of just the centre of double PIV pulse lasers. As the tracer particle, same fluorescent particle with Rohdamin B had been used. With the high-pass optical filter, only the particle images could be recorded. The green light refracted at the bubble interface were not recorded onto the image. The bubble interface had been recorded by the infrared laser as a shadow image, because the high-pass optical filter passed the infrared light. Using only one high-speed camera, the particle image and bubble shadow image had been recorded simultaneously. Figure 9 shows an example instantaneous image. Both of the particle and bubble had been recorded clearly. Please note that the

timing of particle and that of bubble had 50μs difference as shown in Figure 8. Using the image processing technique, bubble and particle images could be separated. For the fluid motion, the particle image had been analysed using PIV technique. The bubble motions had been analysed using the Particle Tracking Velocimetry (PTV). With combining the both information, the flow field and bubble motion had been evaluated.

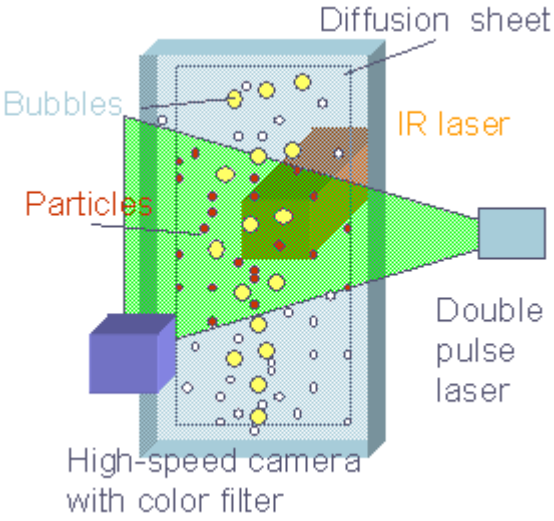

Figure 7 Schematic of bubble experiment (Ishikawa, 2007)

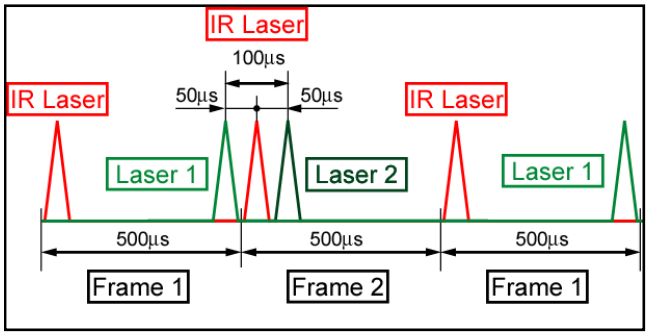

Figure 8 Timing chart for simultaneous measurement (Ishikawa, 2007)

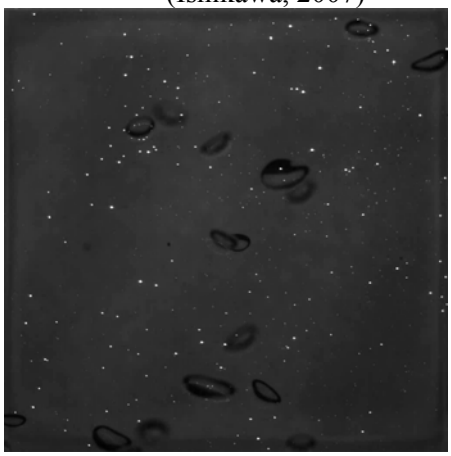

Figure 9 Sample image (Ishikawa, 2007)

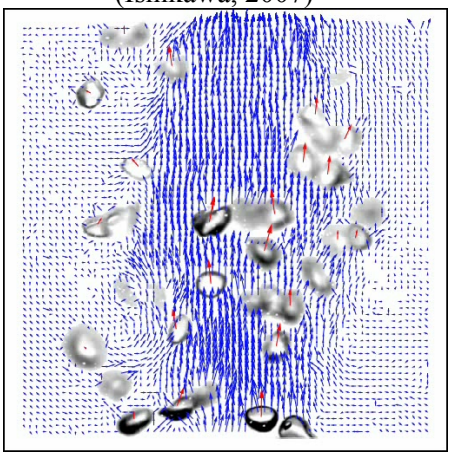

Figure 10 Example of measured velocity (Ishikawa, 2007)

4.2 Proper Orthogonal Decomposition (POD)

Using the high-speed PIV system, the temporal evolution of flow structures had been measured. For turbulent flows, the structures usually mean the "dynamically significant coherent vortical structures". Proper Orthogonal Decomposition (POD) is well known as a non-conditional method for extracting coherent structures from the random turbulent flows. Implementation of POD requests at least 1 spatial dimension measurement of the flow field. The POD analysis was useful to extract the coherent structures especially in the high time-resolved information. The coherent vortical structures in the bubble flow had been studied by 2- and 3-dimensional POD analysis.

Bi et al. (2003) applied the 3D-POD onto the jet flow velocity information taken by the high-speed PIV system. The detail of the 3D-POD had been explained in the reference (Bi et al., 2003). Ishikawa et al. (2010) applied the technique onto the bubble flow. Figure 11 shows the power of the eigen mode for the 3D POD of the bubble flow. Lower spatial and temporal mode had a dominant power. Therefore, taking the lower mode of POD denoted the coherent structures. The POD analysis could be also considered to be the low-pass filter to eliminate the error taken by the experiments. The POD filtered velocity information will be applicable to compare the CFD results. Figure 12 shows the

instantaneous velocity vector map for the liquid phase flow and POD first mode. Because the data had temporal variation, these figures should be shown as movie. In the paper, it is difficult to show the movie, instantaneous velocity map had been shown. Although the lack of temporal information, the first mode structure could clearly express the vortical structures. Usually, the PIV results contain measurement error. Also, the velocity is spatial and temporal filtered vector which represent the surrounding flow field in spatial and temporal directions. The POD filter is the spatial and temporal filter of the measured velocity information to eliminate the noise effects. While the fourier filter just eliminates the high-frequency fluctuation in temporal direction, the POD filter keeps the coherent structures in spatial and temporal directions.

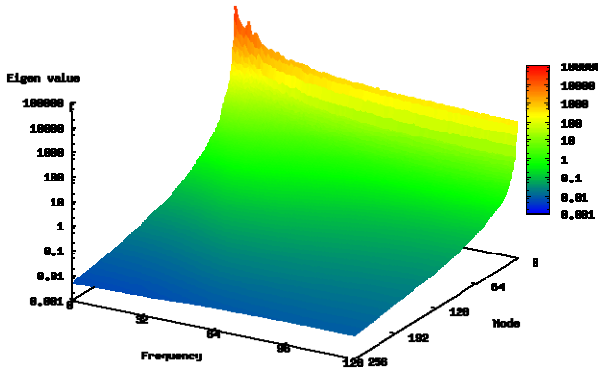

Figure 11 Eigen value for POD modes
(Ishikawa et al., 2010)

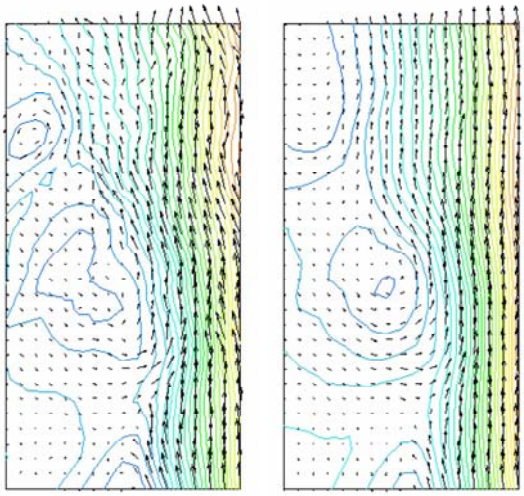

(a) original data (b) 1st mode
Figure 12Velocity map for liquid phase.
(Ishikawa et al., 2010)

5. CONCLUSION

For quantitative measurements and evaluation of two-phase flows, the C-MOS high-speed camera with high-spatial and high-temporal resolutions is the very strong tool. With controlling the camera and pulse laser illuminations, high accurate and high reliable data for CFD verification will be obtained. The temporal variation of the velocity distributions should be filtered using the POD technique to eliminate the noise for the experiments. The pressure distributions around the moving boundary could be also estimated using the velocity information. The quantitative and high-accurate information can be obtained using the high-speed visualization technique. The huge amount of the velocity information in temporal directions can improve the accuracy of the measured data. The data processing technique, i.e., post-processing technique, should be more carefully examined. Then, the verification data could be easily obtained.

REFERENCES

K Okamoto, “Dynamic PIV: a strong tool to resolve the unsteady phenomena,” Particle Image Velocimetry: Recent Improvements (Ed. M Stanislas et al.) Springer, (2003)

K. Shinohara, Y.Sugii, A. Aota, A. Hibara, M. Tokeshi, T. Kitamori and K. Okamoto “High-speed micro-PIV measurements of transient flow in microfluidic devices,” *Meas. Sci. Technol.* Vol. 15 (2004) 1965-1970.

Y. Sugii, S. Nishio, K. Okamoto, A. Nakano, M. Minamiyama and H. Niimi "Red Blood Cell Velocity Field in Rat Mesenteric Arterioles Using Micro PIV Technique," *Int. J. Vascular Biomedical Engineering,* Vol.1, No.1, (2003), 24-31.

JH Jeong, Y. Sugii, M. Minamiyama, K. Okamoto, “Measurement of RBC deformation and velocity in capillaries in vivo,” *Microvasc. Res.* 71 (2006) 212-217

K. Okamoto, “Dynamic Holographic PIV,” International Workshop on Dynamic PIV, Tokyo, March 23, 2004(2004)

TG. Hwang, DH. Doh, K. Okamoto, “4D-PTV - Measurements of an impinged jet with a dynamic 3D-PTV,” *Jounal ofVisualization,* 8 (2005) 245-252

K. Shinohara, Y. Sugii, J.H. Jeong, K. Okamoto, “Development of 3D scanning micro particle image velocimetry system using a piezo actuator,” *Rev. Sci. Instrum.* 76 (2005) 106109

HS Ko, K Ikeda, M Ishikawa, K Okamoto, YJ Kim, “Experimental analysis of high-speed helium jet flow using four-dimensional digital speckle tomography,” *Exp. Fluids* 40 (2006) 442-451

S. Someya, S. Yoshida, K. Okamoto, Y. Li, M. Tange, M.M. Uddin, “Jet ejection from droplets near the Leidenfrost temperature,” *Journal of Visualization*, Vol.13, 41-47 (2010a)

S. Someya, J. Kuwabara, Y. Li and K. Okamoto, “Experimental investigation of a flow-induced oscillating cylinder with two-degrees-of-freesom,” *Nuclear Engineering Design*, (2010b) *in print*

A. Tokuhiro, M. Maekawa, K. Iizuka, K. Hishida and M. Maeda, “Turbulent flow past a bubble and an ellipsoid using shadow-image and PIV techniques,” *Int. J. Multiphase Flow*, 24, 1383-1406 (1998)

M. Ishikawa, “Dynamic PIV measurement of bubble jet flow,” *Journal of Visualization Soc. Japan*, Vol.27, 265-269 (2007) *in Japanese*

W. Bi, Y. Sugii, K. Okamoto, H. Madarame, “Time-resolved proper orthogonal decomposition of the near-field flow of a round jet measured by dynamic particle image velocimetry,” *Meas. Sci. Technol.*, Vol.14, L1-L5 (2003)

M. Ishikawa, K. Irabu, I. Teruya, M. Nitta, “Temporal-spatial characteristic on a bubble jet flow by POD,” *Journal of Visualization Soc. Japan*, Vol.30, Suppl.1, 209-210 (2010) *in Japanese*